ACS NANO
Cite This: *ACS Nano* 2019, 13, 8087−8098
www.acsnano.org

# Tunable Synthesis of Hollow Metal−Nitrogen−Carbon Capsules for Efficient Oxygen Reduction Catalysis in Proton Exchange Membrane Fuel Cells

Hui Yang,[†,‡] Xing Chen,[§] Wan-Ting Chen,[∥] Qing Wang,[∥] Nelly Cantillo Cuello,[⊥] Ayman Nafady,[#] Abdullah M. Al-Enizi,[#] Geoffrey I. N. Waterhouse,[*,∥] Gabriel A. Goenaga,[⊥] Thomas A. Zawodzinski,[⊥] Paul E. Kruger,[¶] John E. Clements,[▲] Jian Zhang,[*,†] He Tian,[*,§] Shane G. Telfer,[*,▲] and Shengqian Ma[*,‡,#]

[†] State Key Laboratory of Structural Chemistry, Fujian Institute of Research on the Structure of Matter, Chinese Academy of Sciences, 350002 Fuzhou, P.R. China

[‡] Department of Chemistry, University of South Florida, 4202 East Fowler Avenue, Tampa, Florida 33620, United States

[§] State Key Laboratory of Silicon Materials, Center of Electron Microscopy, School of Materials Science and Engineering, Zhejiang University, Hangzhou 310027, P.R. China

[∥] MacDiarmid Institute for Advanced Materials and Nanotechnology, School of Chemical Sciences, The University of Auckland, Auckland 1142, New Zealand

[⊥] Chemical and Biomolecular Engineering Department, University of Tennessee, Knoxville, Tennessee 37996, United States

[#] Department of Chemistry, College of Science, King Saud University, Riyadh 11451, Saudi Arabia

[¶] MacDiarmid Institute for Advanced Materials and Nanotechnology, School of Physical and Chemical Sciences, University of Canterbury, Christchurch 8140, New Zealand

[▲] MacDiarmid Institute for Advanced Materials and Nanotechnology, Institute of Fundamental Sciences, Massey University, Palmerston North 4442, New Zealand

*Supporting Information*

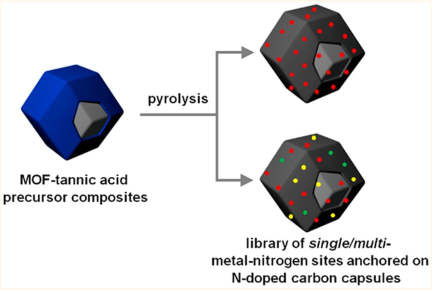

**ABSTRACT:** Atomically dispersed metal catalysts anchored on nitrogen-doped (N-doped) carbons demand attention due to their superior catalytic activity relative to that of metal nanoparticle catalysts in energy storage and conversion processes. Herein, we introduce a simple and versatile strategy for the synthesis of hollow N-doped carbon capsules that contain one or more atomically dispersed metals (denoted as H−M−N$_x$−C and H−M$^{\text{mix}}$−N$_x$−C, respectively, where M = Fe, Co, or Ni). This method utilizes the pyrolysis of nanostructured core−shell precursors produced by coating a zeolitic imidazolate framework core with a metal−tannic acid (M−TA) coordination polymer shell (containing up to three different metal cations). Pyrolysis of these core−shell precursors affords hollow N-doped carbon capsules containing monometal sites (*e.g.*, Fe−N$_x$, CoN$_x$, or Ni−N$_x$) or multimetal sites (Fe/Co−N$_x$, Fe/Ni−N$_x$, Co/Ni−N$_x$, or Fe/Co/Ni−N$_x$). This inventory allowed exploration of the relationship between catalyst composition and electrochemical activity for the oxygen reduction reaction (ORR) in acidic solution. H−Fe−N$_x$−C, H−Co−N$_x$−C, H−FeCo−N$_x$−C, H−FeNi−N$_x$−C, and H−FeCoNi−N$_x$−C were particularly efficient ORR catalysts in acidic solution. Furthermore, the H−Fe−N$_x$−C catalyst exhibited outstanding initial performance when applied as a cathode material in a proton exchange membrane fuel cell. The synthetic methodology introduced here thus provides a convenient route for developing next-generation catalysts based on earth-abundant components.

**KEYWORDS:** *metal−organic framework, metal−nitrogen−carbon, metal single atoms, electrocatalysts, fuel cell*

Carbon-based materials find widespread applications in catalysis due to their low cost, electrical conductivity originating from partial graphitization, and tunable

**Received:** April 15, 2019
**Accepted:** June 19, 2019
**Published:** June 19, 2019

DOI: 10.1021/acsnano.9b02930
*ACS Nano* 2019, 13, 8087−8098

networks of pores and channels which impart high specific surface areas.[1−5] Among the various types of carbon materials available for catalytic reactions, hollow porous carbon capsules (HPCs) are particularly desirable due to their uniform size, shape, and large interior galleries which can be accessed through porous walls, which collectively act to increase the availability of active sites for electron transfer reactions and accelerate mass transfer processes that might otherwise limit catalytic efficiency.[2,6−13]

Recently, porous carbon materials decorated with atomically dispersed metal−nitrogen (M−N$_x$) moieties have emerged as high-performance electrocatalytic materials.[14−17] These catalysts typically consist of metal cations coordinated by nitrogen in porphyrin-like sites anchored on N-doped porous carbon supports. Such N-doped carbon supports frequently comprise stacked two-dimensional (2D) graphene-like sheets. The nitrogen coordination environment about the “single metal atoms” prevents the metals from aggregating into larger clusters and nanoparticles. The highly exposed metal sites (M−N$_x$) allow 100% utilization of the active metal in catalytic processes, thus explaining the superior catalytic efficiencies of M−N$_x$−C catalysts over traditional metal nanoparticle catalysts in many reactions.[14−17] Among M−N$_x$−C catalysts, nonprecious metal containing Fe−N$_x$−C and Co−N$_x$−C have been the most widely studied due to their potential to replace precious metal catalysts in many electrocatalytic reactions.[18,19] Nitrogen doping of carbon is thus crucial for metal binding and the creation of atomically dispersed metal sites, while also enhancing the conductivity and hydrophilicity of carbon electrocatalysts for application in aqueous media.[20−24]

An effective strategy for fabricating M−N$_x$−C materials is to pyrolyze organic precursors rich in both carbon and nitrogen together with an earth-abundant metal source. Traditional synthetic methods toward M−N$_x$−C catalysts employ metal precursors mixed with polymers and organic compounds[18,24−39] or graphene,[40] graphene oxide,[41,42] carbon nitride,[43,44] or carbon nanotubes.[45] In several recent notable contributions, the thermal decomposition of metal−organic frameworks (MOFs) or secondary metal-doped MOFs has been shown to produce Co−N$_x$−C,[46−50] Fe−N$_x$−C,[51−62] and FeCo−N$_x$−C[63−65] catalysts. Although these methods are elegant, general synthetic routes to families of M−N$_x$−C materials with tunable M−N$_x$ centers and hollow structure features (H−M−N$_x$−C) remain rare. This scarcity stems from the fact that the formation of N-doped carbons with good electrical conductivity often demands high temperatures, simultaneously causing the undesirable reduction of metal cations to their metallic state followed by aggregation to form nanoparticles, together with the collapse of the hollow carbon matrices.

We recently pioneered a method to synthesize finely dispersed metal catalysts on hollow N-doped porous carbon capsules (NPCCs). This involved the pyrolysis of composites comprising zeolitic imidazolate framework (ZIF) crystals coated with a metal−tannic acid (M−TA) coordination polymer.[11−13] By this approach, the metal components of the tannic acid coordination polymer were transformed into uniformly dispersed metal nanoparticles on a N-doped carbon support. In the current work, we sought to adapt this methodology to produce hollow N-doped carbon capsules supporting *atomically dispersed* Fe−N$_x$, CoN$_x$, or Ni−N$_x$ sites (as well as multimetal sites, Fe/Co−N$_x$, Fe/Ni−N$_x$, Co/Ni−N$_x$, or Fe/Co/Ni−N$_x$). This approach proved successful, offering a versatile and effective synthetic strategy toward high-performance H−M−N$_x$−C catalysts and electrocatalysts for a diversity of applications.

The preparation of these hollow N-doped carbon capsule-based materials, rich with nitrogen-coordinated metal sites and termed H−M−N$_x$−C or H−M$^{mix}$−N$_x$−C, involves a three-step process (Figure 1). First, ZIF-8 nanocrystals were synthesized and subsequently coated with a thin layer of a potassium−tannic acid coordination polymer to give ZIF-8@K−TA (step I).[11−13] The subsequent exchange of the potassium ions by single metal ions or simultaneously with multiple metal ions was designed to produce core−shell ZIF-8@M−TA or ZIF-8@M$^{mix}$−TA composites (steps II and IV, M$^{mix}$ = a mixture of several different metal ions). Following pyrolysis and then an acid washing step, the metal cations are coordinated by nitrogen donors and uniformly dispersed in the walls of the hollow carbon capsules created *via* pyrolysis of the organic components (step III/route A; step V/route B). We then systematically examined the performance of all these materials as electrocatalysts for the oxygen reduction reaction (ORR) in acidic solution. Many of the as-prepared catalysts exhibited respectable reduction activity evidenced by high onset potentials, high half-wave potentials, and high current densities in acidic media. The H−Fe−N$_x$−C catalyst offered superior performance as a cathode material when tested in an acidic proton exchange membrane fuel cell (PEMFC), demonstrating an excellent an open-circuit voltage as well as high current and power densities.

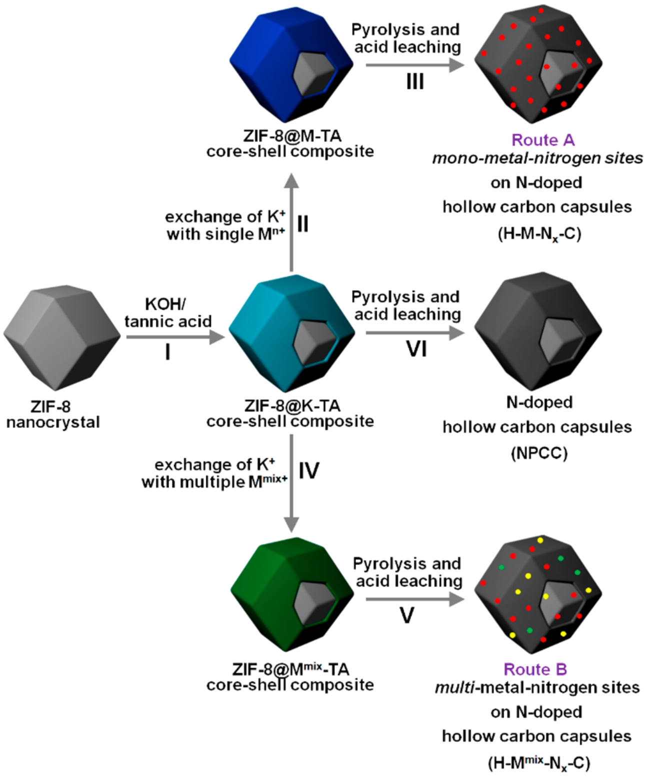

**Figure 1. Schematic of the various routes to hollow N-doped carbon-embedded nitrogen-coordinated metal catalysts (H−M−N$_x$ or H−M$^{mix}$−N$_x$).**

## RESULTS AND DISCUSSION

**Synthesis and Characterization of the H−M−N$_x$−C and H−M$^{mix}$−N$_x$−C Catalysts.** To implement the protocol illustrated in Figure 1, we first prepared ZIF-8 nanocrystals and

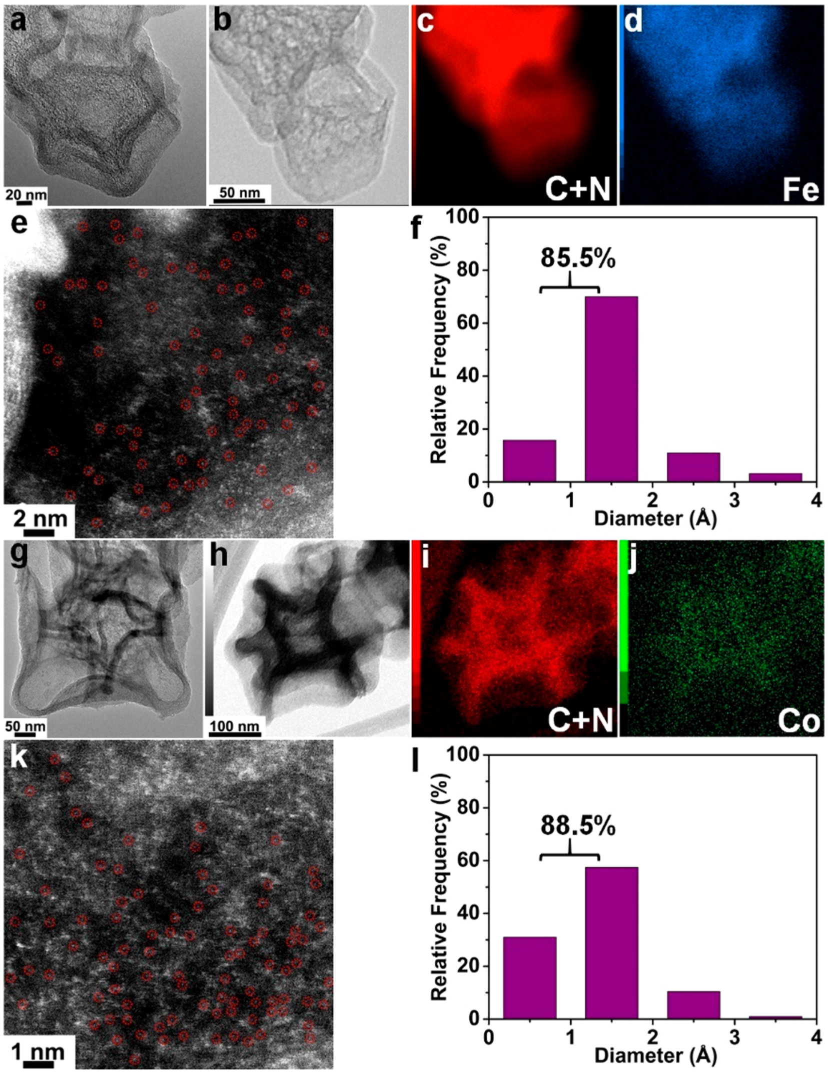

**Figure 2.** (a) TEM image. (b−d) BF-STEM image and corresponding element maps showing the distribution of C, N, and Fe. (e) HAADF-STEM image of H−Fe−$N_x$−C. Single Fe atoms are indicated by red circles. (f) Size distribution of the small spots in panel (e). (g) TEM image. (h−j) BF-STEM image and corresponding element maps showing the distribution of C, N, and Co. (k) Atomic-resolution HAADF-STEM image of H−Co−$N_x$−C. Single Co atoms are highlighted by red circles. (l) Size distribution of the small spots in panel (k).

then deposited a potassium−tannic acid (K−TA) coordination polymer on their surface to deliver a core−shell ZIF-8@K−TA composite (step I).[11−13] Here, the abundant hydroxyl and galloyl groups of tannic acid coordinate potassium cations to create a surface-bound network. The potassium cations in ZIF-8@K−TA were subsequently exchanged for transition metal cations through immersion in a methanolic solution containing the desired metal as a dissolved salt. When a single transition metal salt was used, this postsynthetic cation exchange produced ZIF-8@M−TA with Fe(III), Co(II), and Ni(II) (step II, route A). After pyrolysis under a $N_2$ atmosphere, followed sequentially by acid leaching and an additional pyrolysis treatment, the organic components of ZIF-8@M−TA transform into hollow N-doped porous carbon capsules. The zinc(II) ions of the ZIF disappear from the material due to reduction to zero-valent zinc and subsequent evaporation.[11−13] Meanwhile, the transition metal ions in the tannic acid layer remain strongly coordinated by nitrogen, affording isolated metal cation sites anchored on the capsule walls (step III, route A). These final materials are denoted herein as H−M−$N_x$−C, M = Fe, Co, or Ni. Reduction of the metal cations to the metallic state during the pyrolysis step was largely avoided here due to the low metal loadings (<2 wt %).

We now focus on H−Fe−$N_x$−C as an example to give a detailed structural description of this family of materials. Scanning electron microscopy (SEM) and transmission electron microscopy (TEM) images revealed that H−Fe−$N_x$−C possessed a hollow capsule-like morphology, and its surface becomes much rougher following the pyrolysis treatment (Figure 2a and Figures S6 and S13). Although they would be readily apparent by these methods, no crystalline iron nanoparticles were observed by TEM (Figure 2a) or powder X-ray diffraction (PXRD) (Figure S3). This provides the significant evidence that the iron has deposited in single-atom sites rather than aggregating into larger assemblies. This was confirmed by bright-field scanning transmission electron microscopy (BF-STEM), where Fe and N are shown to be uniformly distributed throughout the capsule walls (Figure 2b−d). We further carried out atomic-resolution high-angle annular dark-field scanning transmission electron microscopy (HAADF-STEM) with the aim of precisely locating the atomically dispersed metals. Numerous bright spots were identified,

DOI: 10.1021/acsnano.9b02930
ACS Nano 2019, 13, 8087−8098

Table 1. Summary of the Elemental Compositions of the As-Synthesized Catalysts[a]

| material | precursor | Fe wt % | Co wt % | Ni wt % | N wt % |
|---|---|---|---|---|---|
| H−Fe−$N_x$−C | ZIF-8@Fe−TA | 1.27 | n/a | n/a | 7.78 |
| H−Co−$N_x$−C | ZIF-8@Co−TA | n/a | 1.8 | n/a | 11.41 |
| H−Ni−$N_x$−C | ZIF-8@Ni−TA | n/a | n/a | 1.4 | 8.93 |
| H−FeCo−$N_x$−C | ZIF-8@FeCo−TA | 0.71 | 0.44 | n/a | 11.36 |
| H−FeNi−$N_x$−C | ZIF-8@FeNi−TA | 0.68 | n/a | 0.35 | 13.37 |
| H−CoNi−$N_x$−C | ZIF-8@CoNi−TA | n/a | 0.54 | 0.38 | 10.86 |
| H−FeCoNi−$N_x$−C | ZIF-8@FeCoNi−TA | 0.45 | 0.36 | 0.4 | 12.76 |

[a] n/a = not applicable. Metal and nitrogen content determined by ICP-AES and element analysis, respectively.

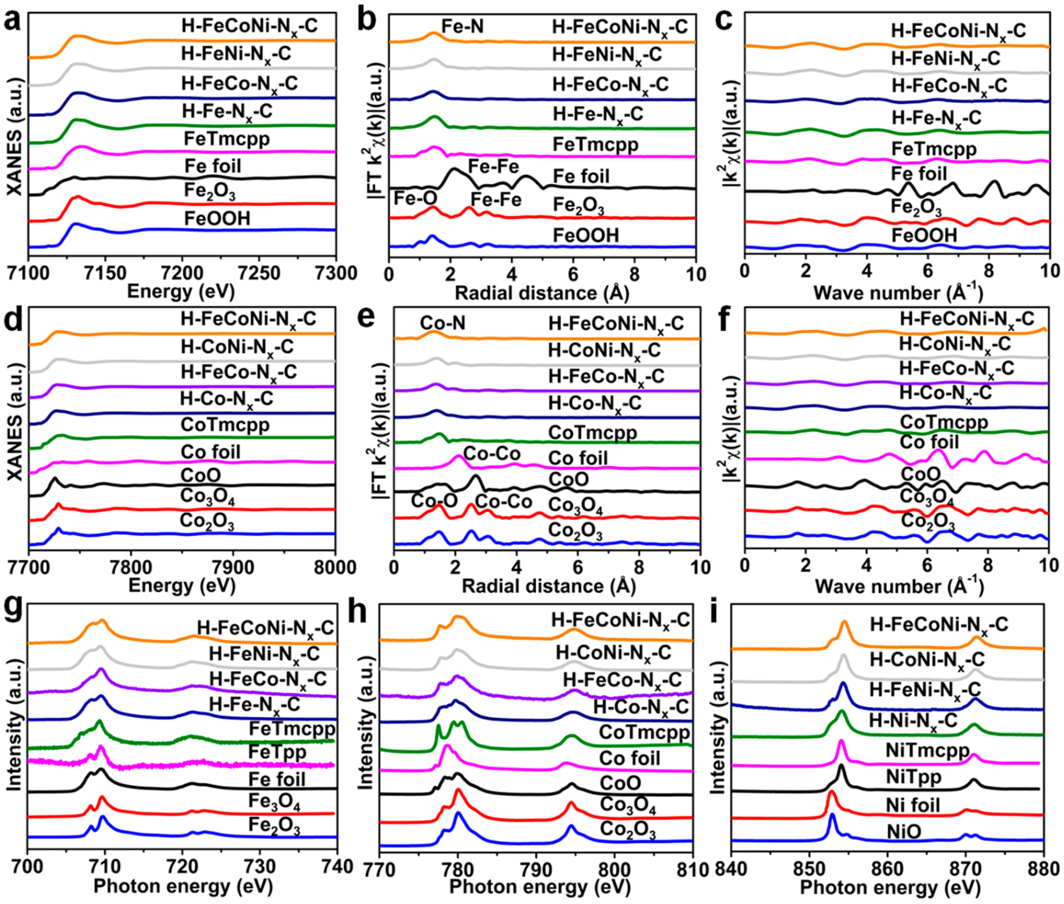

**Figure 3.** (a) XANES spectra. (b,c) Fe K-edge Fourier transform (FT) EXAFS spectra of H−Fe−$N_x$−C together with various Fe standards. (d) XANES spectra. (e,f) Co K-edge (FT) EXAFS spectra of H−Co−$N_x$−C together with various Co standards. (g−i) Fe, Co, and Ni L-edge XANES spectra of different materials: iron(III)-(4-methoxycarbonylphenyl)porphyrin (FeTmcpp); cobalt(II)-(4-methoxycarbonylphenyl)porphyrin (CoTmcpp); nickel(II)-(4-methoxycarbonylphenyl)porphyrin (NiTmcpp); iron(II)-tetraphenyl porphyrin (FeTpp); nickel(II)-tetraphenyl porphyrin (NiTpp).

marked with red cycles in Figure 2e,f, which correspond to the heavier iron atoms. The broad signals observed in the PXRD pattern of H−Fe−$N_x$−C at around 25 and 44° (Figure S3) result from graphitic features of the carbon support. The same features also appeared in the PXRD pattern of the hollow NPCC sample (*i.e.,* the related metal-free material derived from pyrolysis of ZIF-8@K−TA). The Raman spectrum of H−Fe−$N_x$−C exhibited D (1350 $cm^{-1}$) and G (1590 $cm^{-1}$) bands typical of a semigraphitic carbon (Figure S29). On this basis, the carbon capsules were expected to offer good electrical conductivity, as is required for efficient electrocatalysis. H−Fe−$N_x$−C contains 1.2 wt % iron and 8.4 wt % nitrogen, as revealed by inductively coupled plasma atomic emission spectroscopy (ICP-AES) and elemental analysis (EA), respectively (Table 1).

XPS spectra of H−Fe−$N_x$−C revealed iron, carbon, and nitrogen (Figure S30). The N 1s XPS spectrum could be fitted by four components located at 398.3 eV (pyridinic-N), 399.2 eV (pyrrolic-N), 401.1 eV (graphitic-N), and 404.5 eV (quaternary-N). These nitrogen atoms are doped into the carbon support. Because pyridinic and pyrrolic nitrogen atoms can act as donors to iron ions *via* coordination bonds, these observations suggest that Fe occupies sites in the carbon lattice that bear some similarity to molecular species such as iron porphyrins.[57,59,61] In the Fe 2p region, the XPS spectrum shows clear signals attributed to both iron(II) and iron(III). Metallic iron was not detected.

DOI: 10.1021/acsnano.9b02930
*ACS Nano* 2019, 13, 8087−8098

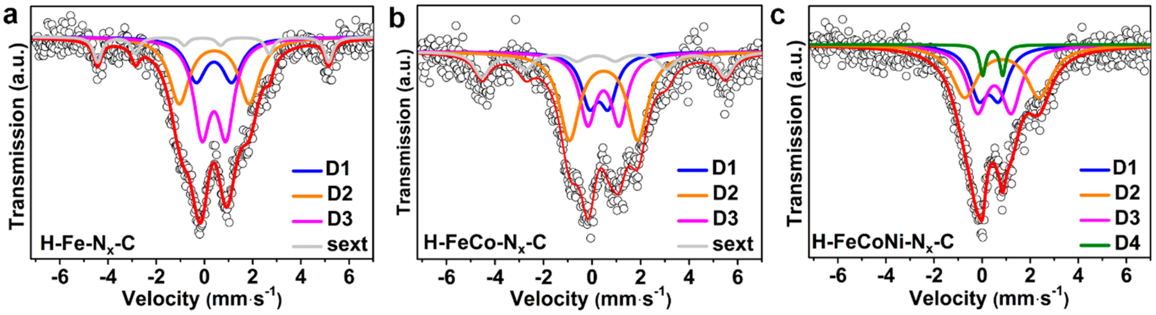

**Figure 4.** $^{57}$**Fe Mössbauer spectra of (a) H−Fe−N$_x$−C, (b) H−FeCo−N$_x$−C, and (c) H−FeCoNi−N$_x$−C.**

X-ray absorption spectroscopy (XAS) was applied to probe the electronic structure of the iron sites in H−Fe−N$_x$−C. Fe foil, $Fe_2O_3$, FeOOH, and FeTmcpp (iron-(4-methoxycarbonylphenyl)porphyrin) were also analyzed as points of comparison (Figure 3a−c). Normalized X-ray absorption near-edge structure (XANES) spectra established that the Fe K-edge absorption edge of H−Fe−N$_x$−C is situated close to that of FeTmcpp, which corroborates the conclusion obtained from XPS that the iron sites in H−Fe−N$_x$−C comprise positively charged iron cations (Figure 3a). Extended X-ray absorption fine structure (EXAFS) analyses enabled deeper investigation of the Fe coordination environment. Markedly different oscillations were observed for H−Fe−N$_x$−C compared to the iron foil, $Fe_2O_3$, and FeOOH references (Figure 3b,c). The oscillations of H−Fe−N$_x$−C at low $k$ are similar to those of the FeTmcpp standard, which is again consistent with the presence of porphyrin-like sites in H−Fe−N$_x$−C. Similar to FeTmcpp, H−Fe−N$_x$−C displays a single well-resolved peak at 1.5 Å in $R$ space, which implies an Fe−N$_x$ scattering path. Fitting the EXAFS data to Fe−N$_x$ species with the iron centers being coordinated by approximately four nitrogen donors with an average Fe−N bond length of 1.972 Å was successful (Figure S37 and Table S1). The Fe L-edge XANES spectrum of H−Fe−N$_x$−C is dominated by distinct sets of peaks ranging from 705 to 712 eV ($L_3$ region, $2p_{3/2} \rightarrow 3d$) and 718 to 726 eV ($L_2$ region, $2p_{1/2} \rightarrow 3d$), which provide further evidence that Fe is present in mixed states ($Fe^{3+}$ and $Fe^{2+}$) (Figure 3g).

To further probe the structure and electronic states of the Fe species in H−Fe−N$_x$−C, we conducted $^{57}$Fe Mössbauer spectroscopy measurements. The spectrum obtained from H−Fe−N$_x$−C can be fitted with three doublets (Figure 4a). $D_1$ and $D_2$ can readily be assigned to porphyrin-like square-planar Fe(II)−$N_4$ coordination sites with Fe(II) in low- and medium-spin states, respectively.[26,66,67] $D_3$ in a low-spin state is assigned to a N−Fe(III)$N_4$−$O_2$ site, supported by density functional theory (DFT) calculations.[26,66−68] These doublets are a well-known signature of active ORR sites in Fe−N$_x$−C catalysts. In addition to the three doublets, the presence of a minor sextet suggests the presence of a very small amount of $\alpha$-Fe or iron carbide in the H−Fe−N$_x$−C sample (the observation of very small metallic Fe clusters is not totally unexpected here given the high pyrolysis temperature of 900 °C used to synthesize H−Fe−N$_x$−C. At such temperatures, coordinating N is also slowly being lost from the N-doped carbons support). The coexistence of Fe−N$_x$ sites with Fe/$Fe_3C$ has been demonstrated to improve ORR performance.[69] However, porous carbon supports containing only Fe and/or $Fe_3C$ nanocrystals exhibit very low ORR activities.[69]

Nitrogen adsorption−desorption isotherms allowed the accessible porosity of H−Fe−N$_x$−C to be probed. The Brunauer−Emmett−Teller (BET) specific surface area for the sample, determined from an isotherm measured at 77 K (Figure 5), was 917 m$^2$ g$^{-1}$ (Table 2). The isotherm showed rapid $N_2$ uptake at low relative pressure ($P/P_0 < 0.1$), followed by a more gradual increase at pressures between $0.1 < P/P_0 < 0.95$, indicating the existence of both micro- and mesopores (Figure 5). The pore size distribution was calculated using a DFT model. The analyses verified that the samples had a hierarchical pore structure, with void diameters clustered around 15 and 27 Å (Figure S25).

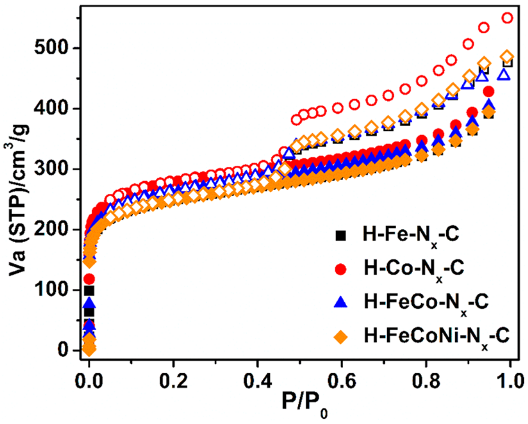

**Figure 5. $N_2$ adsorption (filled symbols) and desorption (open symbols) isotherms measured at 77 K for selected single metal and multi metal catalysts.**

On the basis of complementary experimental techniques, we conclude that H−Fe−N$_x$−C comprises iron cations in the 2+ and 3+ oxidation states coordinated by approximately four nitrogen atoms. These porphyrin-like sites are dispersed in the walls of hollow N-doped carbon capsules. The matrix has an electrically conductive and highly accessible surface area and a network of large pores. This range of characteristics is attractive from the viewpoint of electrocatalysis as the material presents all of its iron sites in a manner that is accessible to incoming small-molecule substrates. Both mass transfer and electron transfer are envisaged to be viable. Given these attractive features, we explored the wider scope of this synthetic approach and its applicability to the fabrication of other catalysts containing isolated M−N$_x$ active sites.

H−Co−N$_x$−C and H−Ni−N$_x$−C were synthesized using a method similar to that used to prepare H−Fe−N$_x$−C, except that cobalt and nickel ions, respectively, were introduced into the tannic acid (M−TA) shell of ZIF-8@M−TA composites. Electron microscopy images and EDS spectra for H−Co−N$_x$−C

DOI: 10.1021/acsnano.9b02930
ACS Nano 2019, 13, 8087−8098

Table 2. Summary of the Surface Areas, Pore Volumes (at 0.95 bar), and ORR Activities of Selected Electrocatalysts[a]

| material | BET surface area ($m^2$ $g^{-1}$) | pore volume ($cm^3$ $g^{-1}$) | onset potential (V *vs* RHE) | half-wave potential (V *vs* RHE) | current density at 0.8 V (*vs* RHE mA $cm^{-2}$) |
|---|---|---|---|---|---|
| H−Fe−$N_x$−C | 917 | 0.611 | 0.950 | 0.77 | 1.68 |
| H−Co−$N_x$−C | 1033 | 0.671 | 0.885 | 0.74 | 0.52 |
| H−Ni−$N_x$−C | 968 | 0.655 | 0.782 | 0.44 | 0 |
| H−FeCo−$N_x$−C | 962 | 0.630 | 0.943 | 0.75 | 1.06 |
| H−FeNi−$N_x$−C | 887 | 0.594 | 0.913 | 0.75 | 0.93 |
| H−CoNi−$N_x$−C | 950 | 0.650 | 0.876 | 0.73 | 0.28 |
| H−FeCoNi−$N_x$−C | 919 | 0.618 | 0.901 | 0.74 | 0.56 |
| NPCC | 1152 | 0.938 | 0.793 | 0.45 | 0 |
| Pt/C (30% of Pt) | n/d | n/d | 1.0 | 0.83 | 3.6 |

[a] n/d = not determined.

and H−Ni−$N_x$−C were consistent with their nominal compositions: ZIF-8@Co−TA (Figure S7) and ZIF-8@Ni−TA (Figure S8). A subsequent pyrolysis step at high temperature (900 °C), acid washing, and a second pyrolysis step resulted in the formation of H−Co−$N_x$−C or H−Ni−$N_x$−C. The PXRD (Figure S3), SEM (Figures S14 and S15), and TEM (Figures 2g and S21) images confirmed that the capsules are hollow and no visible crystalline metal particles exist. BF-STEM and EDX mapping (Figures 2h−j and S21) showed that the C, N, and Co or Ni atoms are dispersed uniformly throughout the capsules. XPS indicated that no cobalt or nickel nanocrystals were present in the samples (Figures S31 and S32). As shown in the atomic-resolution HAADF-STEM image and size distribution panel (Figure 2k,l), the high density of Co single atoms (highlighted by red circles) on the hollow capsules implies a high loading of atomically dispersed Co−$N_x$ sites. The electronic structure of cobalt was also probed by XAS analysis. Co K-edge XANES and EXAFS data for H−Co−$N_x$−C are shown in Figures 3d−f and S38 and closely resemble data collected for CoTmcpp, suggesting a Co−$N_4$ porphyrin-like environment exists in H−Co−$N_x$−C. The XANES spectra at the Co L-edge further again found similarities between H−Co−$N_x$−C and CoTmcpp (Figure 3h), with $Co^{2+}$ being the dominant Co oxidation state present (consistent with XPS analyses, Figure S31). The XAS analysis (Figures 3i and S39) of H−Ni−$N_x$−C also revealed a Ni−$N_x$ coordination environment and demonstrates that Ni(II) single atoms were present in H−Ni−$N_x$−C. The predominance of Ni(II) was also confirmed by XPS (Figure S32).

Inspired by the results above, we decided to explore the versatility of our synthetic strategy by making samples that contained two different metals in $M^{mix}$−$N_x$ sites. This was achieved by retaining our general synthetic methodology and using combinations of (a) iron(III)/cobalt(II), (b) iron(III)/nickel(II), or (c) cobalt(II)/nickel(II) ions in the tannic acid coordination polymer shell layer of the composite precursor (Figure 1, step III, route B). This produced ZIF-8@FeCo−TA, ZIF-8@FeNi−TA, and ZIF-8@CoNi−TA. Microscopy and EDS established that the products possessed the expected elemental compositions (Figures S9−S11).

The subsequent pyrolysis, acid leaching, and second pyrolysis treatment of ZIF-8@FeCo−TA yielded hollow capsules with embedded FeCo−$N_x$ sites (H−FeCo−$N_x$−C). SEM, EDS, and TEM analyses verified hollow capsules comprising Fe/Co−nitrogen-doped carbon (Figures 6a and S16). No large particles are observed in the TEM image, which is consistent with the formation of isolated metal ions rather than larger aggregates. No metallic species were detected by XPS (Figure S33). The HAADF-STEM and EDS elemental maps for H−FeCo−$N_x$−C (Figure 6b−f) indicate that the Fe/Co elements were uniformly distributed over the sample, suggesting that Fe/Co were able to coexist in atomically dispersed form. The atomic-resolution HAADF-STEM image of H−FeCo−$N_x$−C further verified the presence of atomically dispersed Fe/Co−nitrogen-doped active sites (Figure 6g). To probe the electronic structure of the atomically dispersed Fe/Co, XANES and EXAFS measurements were performed. Fe K-edge and L-edge XANES spectra of H−FeCo−$N_x$−C closely resembled data for FeTmcpp and H−Fe−$N_x$−C, whereas the Co K-edge and L-edge data for H−FeCo−$N_x$−C closely matched data for CoTmcpp and H−Co−$N_x$−C, implying that the Fe and Co atoms in H−FeCo−$N_x$−C carried positive charges and existed in porphyrin-like environments (Figure 3a,d). Further, the Fe K-edge EXAFS data for H−FeCo−$N_x$−C align closely with that of H−Fe−$N_x$−C and FeTmcpp, confirming a Fe−N coordination (Figure 3b,c). The Co K-edge spectra showed only one peak at about 1.4 Å in *R* space, attributed to a Co−N scattering path (Figure 3e), which is again very similar to the corresponding spectra of H−Co−$N_x$−C and CoTmcpp. $^{57}$Fe Mössbauer data for H−FeCo−$N_x$−C could be deconvoluted into three doublets and a sextet, which is again similar to data for H−Fe−$N_x$−C (Figure 4b). The doublets D1, D2, and D3 are due to Fe−N species. Combining the XAS and $^{57}$Fe Mössbauer results, it can be concluded that Fe and Co predominantly exist as isolated cations in H−FeCo−$N_x$−C. It might be possible that some Fe or Co atoms are N-bridged together by chemical bonds, but the path length of Fe−N−Co is too similar to that of H−Fe−$N_x$−C and H−Co−$N_x$−C to allow confirmation of this by EXAFS analysis.

We then expanded the scope of the syntheses to include H−FeCo−$N_x$−C analogues, in particular, FeNi−$N_x$−C and H−CoNi−$N_x$−C. PXRD, SEM, TEM, STEM, EDS elemental analysis, XPS, XAS, and Raman spectroscopy (Figure 3 and Figures S17, S18, S22, S23, S29, S34, S35, S40, and S41) revealed a similar structural picture to that of H−FeCo−$N_x$−C: these materials comprised two kinds of atomically dispersed metal atoms decorating the walls of hollow N-doped carbon capsules. ICP-AES and combustion elemental analyses established the metal and nitrogen contents, respectively, in these composites (Table 1). The BET surface areas of these materials ranged from 887 to 962 $m^2$ $g^{-1}$ (Table 2, Figure 5, and Figure S24). Pore size distribution plots derived from the adsorption isotherms showed a hierarchical porosity similar to that seen for the H−M−$N_x$−C analogues (Figures S25 and S26).

To explore the limits of this synthetic approach, we then attempted the preparation of H−FeCoNi−$N_x$−C. This involved incorporating a combination of iron(III)/cobalt(II)/nickel(II) into the tannic acid coordination polymer shell layer of the

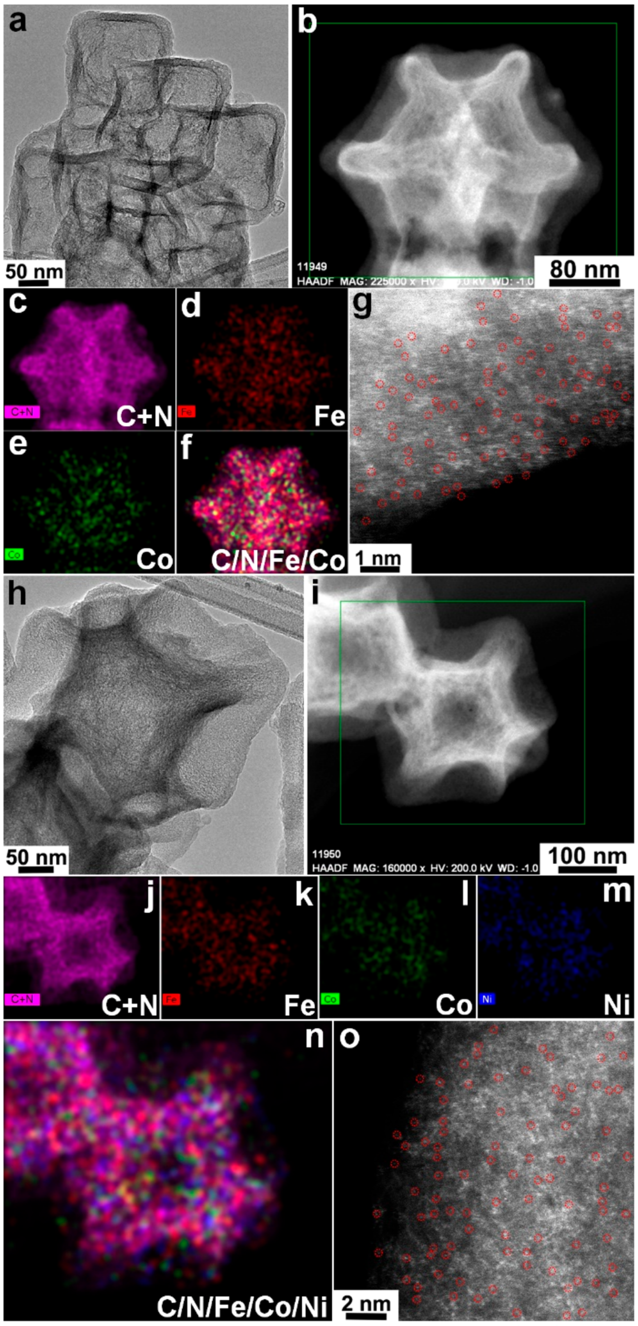

**Figure 6.** (a) TEM image. (b−f) HAADF-STEM image and corresponding element maps examining the distribution of C, N, Fe, and Co. (g) Atomic-resolution HAADF-STEM image of the H−FeCo−$N_x$−C. Single Fe/Co atoms are highlighted by red circles. (h) TEM image. (i−n) HAADF-STEM image and element maps showing the locations of C, N, Fe, Co, and Ni. (o) Atomic-resolution HAADF-STEM image of H−FeCoNi−$N_x$−C. Single Fe/Co/Ni atoms are highlighted by red circles.

composite precursor to produce ZIF-8@FeCoNi−TA. The expected metal components were found by SEM, TEM, and EDS (Figure S12). Subsequent pyrolysis/acid leaching/second pyrolysis treatments resulted in the formation of H−FeCoNi−$N_x$−C. The SEM, TEM, and HAADF-STEM images and associated element maps (Figures 6h−n and S19) demonstrate that the Fe/Co/Ni components were uniformly dispersed over the N-doped hollow capsules. Atomic-resolution HAADF-STEM allowed visualization of the atomically dispersed Fe/Co/Ni atoms in H−FeCoNi−$N_x$−C. As shown in Figure 6o, Fe/Co/Ni single atoms (highlighted by red circles) at high density were visible on the N-doped carbon support, implying a high surface concentration of atomically dispersed $M^{mix}$−$N_x$ (M = Fe, Co and Ni) moieties. XAS analysis showed that iron, cobalt, and nickel were coordinated with nitrogen atoms and dispersed as isolated atoms in H−FeCoNi−$N_x$−C (Figure 3). The electronic structures of Fe, Co, or Ni atoms in H−FeCoNi−$N_x$−C were similar to those of the corresponding metal porphyrins. The $^{57}$Fe Mössbauer spectrum of H−FeCoNi−$N_x$−C was deconvoluted into four doublets, $D_1$−$D_4$, which were all assigned to Fe−N species. No other iron-related phases were observed (Figure 4c). The BET surface area of H−FeCoNi−$N_x$−C calculated from $N_2$ physisorption data taken at 77 K was 919 $m^2\ g^{-1}$ (Figure 5 and Table 2). The corresponding pore size distribution plot revealed hierarchical features characteristic of the other H−M−$N_x$−C and H−$M^{mix}$−$N_x$−C analogues (Figure S25).

**Electrocatalytic $O_2$ Reduction and Proton Exchange Membrane Fuel Cell Performance.** Nitrogen-doped carbon materials (M−$N_x$−C) with embedded metal−nitrogen-doped active sites, such as Fe−$N_x$−C,[28,29,34,51−53,57,70] Co−$N_x$−C,[19,27,47] and Fe−Co−$N_x$−C,[40,64] attract interest as potential alternatives for platinum catalysts in acidic proton exchange membrane fuel cells. The ORR plays a key role in these devices. The synthetic methodology introduced herein offers a platform for the development of alternative oxygen reduction catalysts. To explore the practical potential of our approach, we conducted a series of experiments to assess the electrocatalytic performance of the H−M−$N_x$−C and H−$M^{mix}$−$N_x$−C materials. We first tested their ORR performance in 0.5 M $H_2SO_4$ using a ring rotating disk electrode (RRDE) operated at 1600 rpm. The onset and half-wave potentials and ultimate current densities calculated from these measurements are summarized in Table 2. The performances of H−Fe−$N_x$−C, H−Co−$N_x$−C, and H−FeCo−$N_x$−C were very similar to those of a commercial Pt/C catalyst evaluated under the same conditions and compare favorably against other high-performing ORR electrocatalysts reported in the literature (Table S3). The higher onset and half-wave potentials for H−Fe−$N_x$−C are the result of the special structure of our porous hollow capsule catalyst, which is inherent to our synthetic methodology. The limiting current densities of H−Fe−$N_x$−C, H−Co−$N_x$−C, and H−FeCo−$N_x$−C are larger than those of Pt/C and many other nonprecious metal catalysts (Figure 7a and Table S3). The peroxide yield was used to determine the electron transfer selectivity during ORR. H−Fe−$N_x$−C, H−Co−$N_x$−C, H−FeCo−$N_x$−C, H−FeNi−$N_x$−C, and H−CoNi−$N_x$−C showed a very low peroxide yield of around 15%, and the electron transfer numbers were found to fall between 3.7 and 4. These results suggest the four-electron complete reduction of oxygen to water was preferred (*i.e.*, $O_2 + 4H^+ + 4e^- \rightarrow 2H_2O$ dominates) (Figures 7b and S42). However, further studies are necessary to establish if the ORR occurs through a single four-electron transfer process or sequential two-electron transfer processes, as have been reported by others.[71,72] The Tafel slopes of H−Fe−$N_x$−C, H−Co−$N_x$−C, and H−FeCo−$N_x$−C are 63, 65, and 73 mV $dec^{-1}$, respectively, suggesting that the rate-determining step in the ORR using these catalysts is the migration of adsorbed oxygenated species (Figure S43). NPCC (no metal) and H−Ni−$N_x$−C catalysts exhibited poor ORR activity, confirming that the Co−$N_x$, Fe−$N_x$, or FeCo−$N_x$ sites were important here for realizing a high ORR activity in acidic media.

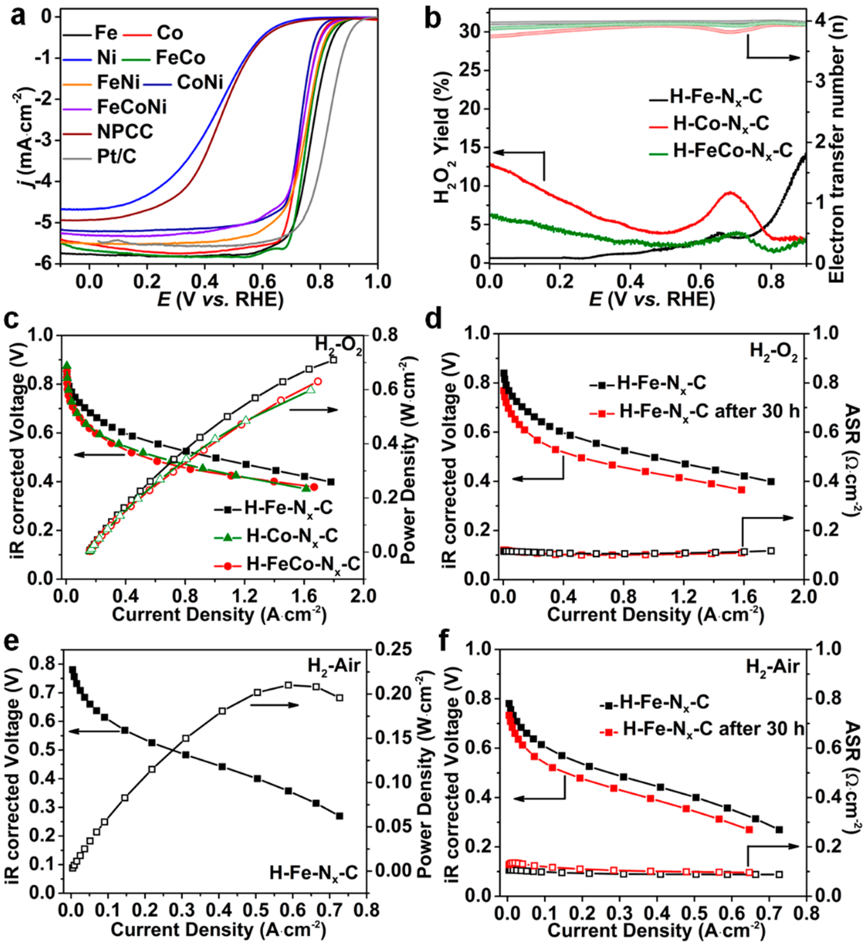

**Figure 7.** (a) Linear sweep voltammetry curves. (b) $H_2O_2$ yield and electron transfer numbers of selected catalysts in 0.5 M $H_2SO_4$ by RRDE tests. (c,d) *I*−*V* polarization and power density curves for $H_2$−$O_2$ PEMFC with H−Fe−$N_x$−C, H−Co−$N_x$−C, and H−FeCo−$N_x$−C as cathode catalysts at 80 °C. (e,f) $H_2$−air PEMFC performance with H−Fe−$N_x$−C as the cathode catalyst.

In view of the excellent electrochemical properties of these alternative catalysts, we also carried out PEMFC performance tests on H−Fe−$N_x$−C, H−Co−$N_x$−C, and H−FeCo−$N_x$−C. These materials were utilized as cathode materials for the oxygen reduction reaction. Polarization curves were collected on 5 $cm^2$ membrane electrode assemblies at 80 °C and back pressures of 29.4 psia, using absolute oxygen as the gas feed to the cathode catalysts in the fuel cells. A commercial Vulcan XC72 carbon-supported platinum catalyst was employed as the anode for the $H_2$ oxidation reaction.

Under a catalyst loading of 2 mg $cm^{-2}$, the open-circuit voltages (OCV) of H−Fe−$N_x$−C, H−Co−$N_x$−C, and H−FeCo−$N_x$−C in these $H_2/O_2$ fuel cells were 0.85, 0.86, and 0.88 V, respectively (Figure 7c). At a working voltage of 0.43 V, a current density of 1.55 A $cm^{-2}$ and a peak power density of 0.655 W $cm^{-2}$ were achieved using a H−Fe−$N_x$−C-based membrane electrode assembly (MEA), which are higher than those of the MEAs made with H−Co−$N_x$−C (0.103 A $cm^{-2}$ and 0.457 W $cm^{-2}$) and H−FeCo−$N_x$−C (0.104 A $cm^{-2}$ and 0.459 W $cm^{-2}$). The maximum power density of the cell constructed with H−Fe−$N_x$−C was 0.71 W $cm^{-2}$ at 0.4 V, far superior to the values of 0.63 W $cm^{-2}$ at 0.38 V for H−Co−$N_x$−C and 0.6 W $cm^{-2}$ at 0.37 V for H−FeCo−$N_x$−C (Figure 7c). These values are comparable to those of other reported ZIF-derived noble metal free catalysts for PEMFCs (Table S4). The PEMFC performance of H−Fe−$N_x$−C-based cathodes with different catalyst mass loadings was also investigated. The cathode with a 2 mg $cm^{-2}$ loading of H−Fe−$N_x$−C showed the highest OCV and power density (Figure S45). The durability of the cell (with 2 mg $cm^{-2}$ of H−Fe−$N_x$−C electrocatalyst) was explored by holding it at a constant voltage of 0.7 V and collecting polarization curves before and after operation over a period of 30 h (Figure 7d). A steady decay of fuel cell OCV and current density were observed. Thus, improvements in stability are required before this material can be used in real applications. H−Fe−$N_x$−C also showed relatively low performance in a $H_2$−air battery test (Figure 7e,f).

Taken together, these experimental results reveal valuable information about our general synthetic methodology that involves introducing transition metal cations into a core−shell polymer composite precursor and then pyrolysis to deliver hollow metal−nitrogen-doped porous carbon catalysts. These catalysts provide abundant single metal sites (Fe, Co, or Ni) or a plurality of metal sites (Fe/Co, Fe/Ni, or Fe/Co/Ni), which are anchored on the walls of hollow nitrogen-doped porous carbon capsules created by the pyrolysis of the organic matter in the composite precursor. The metal−nitrogen sites in these materials were identified as porphyrin-like sites by various advanced characterization techniques. The hollow nitrogen-doped carbon matrix has an electrically conductive and highly accessible surface area (>900 $m^2$ $g^{-1}$) and a network of large pores. These structural features allow for efficient mass transport and electron transfer. This range of characteristics is attractive

DOI: 10.1021/acsnano.9b02930
ACS Nano 2019, 13, 8087−8098

from the viewpoint of electrocatalysis. To demonstrate the utility of our synthetic method for producing a broad library of nitrogen-doped porous-carbon-supporting metal−nitrogen active sites, we tested their electrocatalytic performances toward the ORR in acidic PEMFCs. We identified a functional relationship between the type of metal−nitrogen sites and their electrochemical activity. This report highlights how a single synthetic strategy can create diverse libraries of porous carbon catalysts supporting metal−single atom catalysts. Such versatility allows the fast synthesis and screening of diverse electrocatalysts for target applications. Improvements in overall catalytic activities and stability are demanded for practical applications, which may be achievable through judicious selection of the metals and relative proportions of individual metal components in the catalysts.

## CONCLUSION

In summary, we have discovered a simple and versatile synthetic strategy for the realization of hollow porous carbon capsule-embedded nitrogen-coordinated metal catalysts. This strategy is applicable for the synthesis of single metal catalysts (Fe, Co, or Ni) or multiple metal catalysts (Fe/Co, Fe/Ni, Co/Ni, or Fe/Co/Ni) rich with atomically dispersed metal (M−$N_x$) active sites. The obtained H−Fe−$N_x$−C, H−Co−$N_x$−C, and H−FeCo−$N_x$−C catalysts showed very respectable ORR performance in acid media, offering high onset and high half-wave potentials and high current densities. The H−Fe−$N_x$−C catalyst further demonstrated excellent initial activity in a proton exchange membrane fuel cell. This general synthetic strategy creates avenues for the rational design of highly active metal−nitrogen−porous carbon catalysts for electrocatalytic applications and efficient energy conversion.

## EXPERIMENTAL METHODS

Full experimental methods are summarized in the Supporting Information.

**Synthesis of ZIF-8 Nanocrystals.** ZIF-8 nanocrystals were synthesized by following a reported route with minute modifications.[73] For a typical experiment, 4 g of 2-methylimidazole (2-mim) was dissolved in 60 mL of methanol (MeOH). Next, 1.68 g of $Zn(NO_3)_2\cdot 6H_2O$ dissolved in 20 mL of MeOH was subsequently added to the 2-mim/MeOH solution. The mixture was then stirred for 1 h and incubated for another 24 h at 25 °C. The product was washed several times with deionized water and MeOH, collected by centrifugation, and placed in a vacuum oven to dry at 25 °C.

**Synthesis of ZIF-8@K−TA.** The ZIF-8@K−TA was synthesized by using our previously reported method.[11,12] To obtain a solid ZIF-8@K−TA material, 200 mg of ZIF-8 nanocrystals was dispersed in 10 mL of deionized water in a 100 mL conical flask. This was followed by addition of 3 mL of TA/KOH/$H_2O$ solution (24 mM, pH 8) to the ZIF-8 nanocrystal suspension. After being stirred for 5 min, the product was collected by centrifugation, washed several times with deionized water and MeOH, and then placed in an oven to dry.

**Synthesis of ZIF-8@M−TA and ZIF-8@$M^{mix}$−TA Composites.** The ZIF-8@K−TA was dispersed in a methanolic solution (30 mL) of $Fe(NO_3)_3\cdot 9H_2O$ (60 mg). After being stirred for 2 h, the product was collected by centrifugation, washed several times with deionized water and MeOH, and then placed in a vacuum oven to dry. Other composites were synthesized *via* similar synthetic routes: ZIF-8@Co−TA: $Co(NO_3)_2\cdot 6H_2O$ (60 mg); ZIF-8@Ni−TA: $Ni(NO_3)_2\cdot 6H_2O$ (60 mg); ZIF-8@FeCo−TA: $Fe(NO_3)_3\cdot 9H_2O$ (30 mg)/$Co(NO_3)_2\cdot 6H_2O$ (30 mg); ZIF-8@FeNi−TA: $Fe(NO_3)_3\cdot 9H_2O$ (30 mg)/$Ni(NO_3)_2\cdot 6H_2O$ (30 mg); ZIF-8@CoNi−TA: $Co(NO_3)_2\cdot 6H_2O$ (30 mg)/$Ni(NO_3)_2\cdot 6H_2O$ (30 mg); ZIF-8@FeCoNi−TA: $Fe(NO_3)_3\cdot 9H_2O$ (20 mg)/$Co(NO_3)_2\cdot 6H_2O$ (20 mg)/$Ni(NO_3)_2\cdot 6H_2O$ (20 mg).

**Synthesis of H−M−$N_x$−C and H−$M^{mix}$−$N_x$−C Catalysts.** ZIF-8@Fe−TA was placed in a heating zone within a tubular furnace. The pyrolysis of ZIF-8@Fe−TA was conducted under a nitrogen flow and heated to 900 °C with a ramp rate of 1 $°C\cdot min^{-1}$. The product was obtained by pyrolysis for another 3 h at 900 °C. The black product was then immersed in 0.5 M $H_2SO_4$ at 90 °C for 12 h, followed by washing with deionized water. After being dried at 90 °C in a vacuum oven, the powder was heat-treated at 900 °C under a $N_2$ atmosphere for 3 h to obtain the final product, termed H−Fe−$N_x$−C. Other catalysts, H−Co−$N_x$−C, H−Ni−$N_x$−C, H−FeCo−$N_x$−C, H−FeNi−$N_x$−C, H−CoNi−$N_x$−C, and H−FeCoNi−$N_x$−C, were prepared from the corresponding precursor using the same protocol.

## ASSOCIATED CONTENT

### Ⓢ Supporting Information

The Supporting Information is available free of charge on the ACS Publications website at DOI: 10.1021/acsnano.9b02930.

> Materials, experimental methods, and additional characterization data (powder X-ray diffraction, SEM, EDS, TEM, STEM, Raman, gas sorption analysis, pore size distribution calculations, FTIR, XPS, XAS, and electrochemical related curves and calculations) (PDF)

## AUTHOR INFORMATION

### Corresponding Authors

*E-mail: g.waterhouse@auckland.ac.nz.
*E-mail: zhj@fjirsm.ac.cn.
*E-mail: hetian@zju.edu.cn.
*E-mail: s.telfer@massey.ac.nz.
*E-mail: sqma@usf.edu.

### ORCID

Geoffrey I. N. Waterhouse: 0000-0002-3296-3093
Paul E. Kruger: 0000-0003-4847-6780
Jian Zhang: 0000-0003-3373-9621
Shane G. Telfer: 0000-0003-1596-6652
Shengqian Ma: 0000-0002-1897-7069

### Notes

The authors declare no competing financial interest.

## ACKNOWLEDGMENTS

We gratefully acknowledge the financial support from NSFC (21425102, 11474249, and 21521061), the Strategic Priority Research Program of the Chinese Academy of Sciences (XDB20000000), the Ministry of Business, Innovation and Employment for a Catalyst Fund grant (MAUX 1609), and the University of South Florida. The authors also extend their appreciation to the Distinguished Scientist Fellowship Program (DSFP) at King Saud University for partial funding of this work. We thank Dr. Yunling Liu for recording the $^{57}$Fe Mössbauer spectra, Dr. Jisue Moon for XAS fitting analysis, and Dr. Tian-You Zhou for his inputs on the graphics. We also acknowledge support from the Australian Synchrotron, part of ANSTO, and the Stanford Synchrotron Radiation Lightsource (SSRL) for providing beam time.

## REFERENCES

(1) Benzigar, M. R.; Talapaneni, S. N.; Joseph, S.; Ramadass, K.; Singh, G.; Scaranto, J.; Ravon, U.; Al-Bahily, K.; Vinu, A. Recent Advances in Functionalized Micro and Mesoporous Carbon Materials: Synthesis and Applications. *Chem. Soc. Rev.* **2018**, *47*, 2680−2721.

(2) Zhang, P.; Zhu, H.; Dai, S. Porous Carbon Supports: Recent Advances with Various Morphologies and Compositions. *ChemCatChem* **2015**, *7*, 2788−2805.

(3) Lee, J.; Kim, J.; Hyeon, T. Recent Progress in the Synthesis of Porous Carbon Materials. *Adv. Mater.* **2006**, *18*, 2073−2094.

(4) Zhi, L.; Wang, J.; Cui, G.; Kastler, M.; Schmaltz, B.; Kolb, U.; Jonas, U.; Müllen, K. From Well-Defined Carbon-Rich Precursors to Monodisperse Carbon Particles with Hierarchic Structures. *Adv. Mater.* **2007**, *19*, 1849−1853.

(5) Xia, Y.; Yang, Z.; Mokaya, R. Templated Nanoscale Porous Carbons. *Nanoscale* **2010**, *2*, 639−59.

(6) Galeano, C.; Meier, J. C.; Soorholtz, M.; Bongard, H.; Baldizzone, C.; Mayrhofer, K. J. J.; Schüth, F. Nitrogen-Doped Hollow Carbon Spheres as a Support for Platinum-Based Electrocatalysts. *ACS Catal.* **2014**, *4*, 3856−3868.

(7) Galeano, C.; Baldizzone, C.; Bongard, H.; Spliethoff, B.; Weidenthaler, C.; Meier, J. C.; Mayrhofer, K. J. J.; Schüth, F. Carbon-Based Yolk-Shell Materials for Fuel Cell Applications. *Adv. Funct. Mater.* **2014**, *24*, 220−232.

(8) Ikeda, S.; Ishino, S.; Harada, T.; Okamoto, N.; Sakata, T.; Mori, H.; Kuwabata, S.; Torimoto, T.; Matsumura, M. Ligand-Free Platinum Nanoparticles Encapsulated in a Hollow Porous Carbon Shell as a Highly Active Heterogeneous Hydrogenation Catalyst. *Angew. Chem., Int. Ed.* **2006**, *45*, 7063−7066.

(9) Liu, R.; Mahurin, S. M.; Li, C.; Unocic, R. R.; Idrobo, J. C.; Gao, H.; Pennycook, S. J.; Dai, S. Dopamine as a Carbon Source: the Controlled Synthesis of Hollow Carbon Spheres and Yolk-Structured Carbon Nanocomposites. *Angew. Chem., Int. Ed.* **2011**, *50*, 6799−6802.

(10) Wang, G. H.; Hilgert, J.; Richter, F. H.; Wang, F.; Bongard, H. J.; Spliethoff, B.; Weidenthaler, C.; Schuth, F. Platinum-Cobalt Bimetallic Nanoparticles in Hollow Carbon Nanospheres for Hydrogenolysis of 5-Hydroxymethylfurfural. *Nat. Mater.* **2014**, *13*, 293−300.

(11) Yang, H.; Bradley, S. J.; Chan, A.; Waterhouse, G. I.; Nann, T.; Kruger, P. E.; Telfer, S. G. Catalytically Active Bimetallic Nanoparticles Supported on Porous Carbon Capsules Derived From Metal-Organic Framework Composites. *J. Am. Chem. Soc.* **2016**, *138*, 11872−11881.

(12) Yang, H.; Bradley, S. J.; Wu, X.; Chan, A.; Waterhouse, G. I. N.; Nann, T.; Zhang, J.; Kruger, P. E.; Ma, S.; Telfer, S. G. General Synthetic Strategy for Libraries of Supported Multicomponent Metal Nanoparticles. *ACS Nano* **2018**, *12*, 4594−4604.

(13) Guo, F.; Yang, H.; Liu, L.; Han, Y.; Al-Enizi, A. M.; Nafady, A.; Kruger, P. E.; Telfer, S. G.; Ma, S. Hollow Capsules of Doped Carbon Incorporating Metal@Metal Sulfide and Metal@Metal Oxide Core−Shell Nanoparticles Derived from Metal−Organic Framework Composites for Efficient Oxygen Electrocatalysis. *J. Mater. Chem. A* **2019**, *7*, 3624−3631.

(14) Shen, M.; Wei, C.; Ai, K.; Lu, L. Transition Metal−Nitrogen−Carbon Nanostructured Catalysts for the Oxygen Reduction Reaction: From Mechanistic Insights to Structural Optimization. *Nano Res.* **2017**, *10*, 1449−1470.

(15) Wu, G.; Zelenay, P. Nanostructured Nonprecious Metal Catalysts For Oxygen Reduction Reaction. *Acc. Chem. Res.* **2013**, *46*, 1878−89.

(16) Masa, J.; Xia, W.; Muhler, M.; Schuhmann, W. On the Role of Metals in Nitrogen-Doped Carbon Electrocatalysts for Oxygen Reduction. *Angew. Chem., Int. Ed.* **2015**, *54*, 10102−10120.

(17) Mamtani, K.; Ozkan, U. S. Heteroatom-Doped Carbon Nanostructures as Oxygen Reduction Reaction Catalysts in Acidic Media: An Overview. *Catal. Lett.* **2015**, *145*, 436−450.

(18) Wu, G.; More, K. L.; Johnston, C. M.; Zelenay, P. High-Performance Electrocatalysts for Oxygen Reduction Derived from Polyaniline, Iron, and Cobalt. *Science* **2011**, *332*, 443−447.

(19) Bashyam, R.; Zelenay, P. A Class of Non-Precious Metal Composite Catalysts for Fuel Cells. *Nature* **2006**, *443*, 63−66.

(20) Ding, W.; Wei, Z.; Chen, S.; Qi, X.; Yang, T.; Hu, J.; Wang, D.; Wan, L. J.; Alvi, S. F.; Li, L. Space-Confinement-Induced Synthesis of Pyridinic- and Pyrrolic-Nitrogen-Doped Graphene for the Catalysis of Oxygen Reduction. *Angew. Chem., Int. Ed.* **2013**, *52*, 11755−11759.

(21) Tang, J.; Liu, J.; Li, C.; Li, Y.; Tade, M. O.; Dai, S.; Yamauchi, Y. Synthesis of Nitrogen-Doped Mesoporous Carbon Spheres with Extra-Large Pores Through Assembly of Diblock Copolymer Micelles. *Angew. Chem., Int. Ed.* **2015**, *54*, 588−593.

(22) Lv, Q.; Si, W.; He, J.; Sun, L.; Zhang, C.; Wang, N.; Yang, Z.; Li, X.; Wang, X.; Deng, W.; Long, Y.; Huang, C.; Li, Y. Selectively Nitrogen-Doped Carbon Materials as Superior Metal-Free Catalysts for Oxygen Reduction. *Nat. Commun.* **2018**, *9*, 3376.

(23) Zhao, Y.; Wan, J.; Yao, H.; Zhang, L.; Lin, K.; Wang, L.; Yang, N.; Liu, D.; Song, L.; Zhu, J.; Gu, L.; Liu, L.; Zhao, H.; Li, Y.; Wang, D. Few-Layer Graphdiyne Doped with Sp-hybridized Nitrogen Atoms at Acetylenic Sites for Oxygen Reduction Electrocatalysis. *Nat. Chem.* **2018**, *10*, 924−931.

(24) Zhao, Y.; Watanabe, K.; Hashimoto, K. Self-Supporting Oxygen Reduction Electrocatalysts Made from a Nitrogen-Rich Network Polymer. *J. Am. Chem. Soc.* **2012**, *134*, 19528−19531.

(25) Serov, A.; Artyushkova, K.; Atanassov, P. Fe-N-C Oxygen Reduction Fuel Cell Catalyst Derived from Carbendazim: Synthesis, Structure, and Reactivity. *Adv. Eng. Mater.* **2014**, *4*, 1301735.

(26) Sahraie, N. R.; Kramm, U. I.; Steinberg, J.; Zhang, Y.; Thomas, A.; Reier, T.; Paraknowitsch, J. P.; Strasser, P. Quantifying the Rensity and Utilization of Active Sites in Non-Precious Metal Oxygen Electroreduction Catalysts. *Nat. Commun.* **2015**, *6*, 8618.

(27) Chang, S.-T.; Wang, C.-H.; Du, H.-Y.; Hsu, H.-C.; Kang, C.-M.; Chen, C.-C.; Wu, J. C. S.; Yen, S.-C.; Huang, W.-F.; Chen, L.-C.; Lin, M. C.; Chen, K.-H. Vitalizing Fuel Cells with Vitamins: Pyrolyzed Vitamin $B_{12}$ as a Non-Precious Catalyst for Enhanced Oxygen Reduction Reaction of Polymer Electrolyte Fuel Cells. *Energy Environ. Sci.* **2012**, *5*, 5305−5314.

(28) Fu, X.; Zamani, P.; Choi, J. Y.; Hassan, F. M.; Jiang, G.; Higgins, D. C.; Zhang, Y.; Hoque, M. A.; Chen, Z. *In Situ* Polymer Graphenization Ingrained with Nanoporosity in a Nitrogenous Electrocatalyst Boosting the Performance of Polymer-Electrolyte-Membrane Fuel Cells. *Adv. Mater.* **2017**, *29*, 1604456.

(29) Meng, F. L.; Wang, Z. L.; Zhong, H. X.; Wang, J.; Yan, J. M.; Zhang, X. B. Reactive Multifunctional Template-Induced Preparation of Fe-N-Doped Mesoporous Carbon Microspheres Towards Highly Efficient Electrocatalysts for Oxygen Reduction. *Adv. Mater.* **2016**, *28*, 7948−7955.

(30) Han, Y.; Wang, Y. G.; Chen, W.; Xu, R.; Zheng, L.; Zhang, J.; Luo, J.; Shen, R. A.; Zhu, Y.; Cheong, W. C.; Chen, C.; Peng, Q.; Wang, D.; Li, Y. Hollow N-Doped Carbon Spheres with Isolated Cobalt Single Atomic Sites: Superior Electrocatalysts for Oxygen Reduction. *J. Am. Chem. Soc.* **2017**, *139*, 17269−17272.

(31) Xiao, M.; Zhu, J.; Feng, L.; Liu, C.; Xing, W. Meso/Macroporous Nitrogen-Doped Carbon Architectures with Iron Carbide Encapsulated in Graphitic Layers as an Efficient and Robust Catalyst for the Oxygen Reduction Reaction in Both Acidic and Alkaline solutions. *Adv. Mater.* **2015**, *27*, 2521−2527.

(32) Wang, Y. C.; Lai, Y. J.; Song, L.; Zhou, Z. Y.; Liu, J. G.; Wang, Q.; Yang, X. D.; Chen, C.; Shi, W.; Zheng, Y. P.; Rauf, M.; Sun, S. G. S-Doping of an Fe/N/C ORR Catalyst for Polymer Electrolyte Membrane Fuel Cells with High Power Density. *Angew. Chem., Int. Ed.* **2015**, *54*, 9907−9910.

(33) Chen, Y.; Li, Z.; Zhu, Y.; Sun, D.; Liu, X.; Xu, L.; Tang, Y. Atomic Fe Dispersed on N-Doped Carbon Hollow Nanospheres for High-Efficiency Electrocatalytic Oxygen Reduction. *Adv. Mater.* **2019**, *31*, 1806312.

(34) Yuan, S.; Shui, J. L.; Grabstanowicz, L.; Chen, C.; Commet, S.; Reprogle, B.; Xu, T.; Yu, L.; Liu, D. J. A Highly Active and Support-Free Oxygen Reduction Catalyst Prepared from Ultrahigh-Surface-Area Porous Polyporphyrin. *Angew. Chem., Int. Ed.* **2013**, *52*, 8349−8353.

(35) Workman, M. J.; Serov, A.; Tsui, L.-k.; Atanassov, P.; Artyushkova, K. Fe−N−C Catalyst Graphitic Layer Structure and Fuel Cell Performance. *ACS Energy Lett.* **2017**, *2*, 1489−1493.

(36) Liang, H. W.; Wei, W.; Wu, Z. S.; Feng, X.; Mullen, K. Mesoporous Metal-Nitrogen-Doped Carbon Electrocatalysts for Highly Efficient Oxygen Reduction Reaction. *J. Am. Chem. Soc.* **2013**, *135*, 16002−16005.

(37) Xie, J.; Li, B. Q.; Peng, H. J.; Song, Y. W.; Li, J. X.; Zhang, Z. W.; Zhang, Q. From Supramolecular Species to Self-Templated Porous Carbon and Metal-Doped Carbon for Oxygen Reduction Reaction Catalysts. *Angew. Chem., Int. Ed.* **2019**, *58*, 4963−4967.

(38) Zhang, Z.; Dou, M.; Liu, H.; Dai, L.; Wang, F. A Facile Route to Bimetal and Nitrogen-Codoped 3D Porous Graphitic Carbon Networks for Efficient Oxygen Reduction. *Small* **2016**, *12*, 4193−4199.

(39) Liang, H. W.; Bruller, S.; Dong, R.; Zhang, J.; Feng, X.; Mullen, K. Molecular Metal-$N_x$ Centres in Porous Carbon for Electrocatalytic Hydrogen Evolution. *Nat. Commun.* **2015**, *6*, 7992.

(40) Palaniselvam, T.; Kashyap, V.; Bhange, S. N.; Baek, J.-B.; Kurungot, S. Nanoporous Graphene Enriched with Fe/Co-N Active Sites as a Promising Oxygen Reduction Electrocatalyst for Anion Exchange Membrane Fuel Cells. *Adv. Funct. Mater.* **2016**, *26*, 2150−2162.

(41) Fei, H. L.; Dong, J. C.; Feng, Y. X.; Allen, C. S.; Wan, C. Z.; Volosskiy, B.; Li, M. F.; Zhao, Z. P.; Wang, Y. L.; Sun, H. T.; An, P. F.; Chen, W. X.; Guo, Z. Y.; Lee, C.; Chen, D. L.; Shakir, I.; Liu, M. J.; Hu, T. D.; Li, Y. D.; Kirkland, A. I.; Duan, X. F.; Huang, Y. General Synthesis and Definitive Structural Identification of MN4C4 Single-Atom Catalysts with Tunable Electrocatalytic Activities. *Nat. Catal.* **2018**, *1*, 63−72.

(42) Fei, H.; Dong, J.; Arellano-Jimenez, M. J.; Ye, G.; Dong Kim, N.; Samuel, E. L.; Peng, Z.; Zhu, Z.; Qin, F.; Bao, J.; Yacaman, M. J.; Ajayan, P. M.; Chen, D.; Tour, J. M. Atomic Cobalt on Nitrogen-Doped Graphene for Hydrogen Generation. *Nat. Commun.* **2015**, *6*, 8668.

(43) Zhao, L.; Zhang, Y.; Huang, L. B.; Liu, X. Z.; Zhang, Q. H.; He, C.; Wu, Z. Y.; Zhang, L. J.; Wu, J.; Yang, W.; Gu, L.; Hu, J. S.; Wan, L. J. Cascade Anchoring Strategy for General Mass Production of High-Loading Single-Atomic Metal-Nitrogen Catalysts. *Nat. Commun.* **2019**, *10*, 1278.

(44) Lee, J. H.; Park, M. J.; Yoo, S. J.; Jang, J. H.; Kim, H. J.; Nam, S. W.; Yoon, C. W.; Kim, J. Y. A Highly Active and Durable Co-N-C Electrocatalyst Synthesized Using Exfoliated Graphitic Carbon Nitride Nanosheets. *Nanoscale* **2015**, *7*, 10334−10339.

(45) Sa, Y. J.; Seo, D. J.; Woo, J.; Lim, J. T.; Cheon, J. Y.; Yang, S. Y.; Lee, J. M.; Kang, D.; Shin, T. J.; Shin, H. S.; Jeong, H. Y.; Kim, C. S.; Kim, M. G.; Kim, T. Y.; Joo, S. H. A General Approach to Preferential Formation of Active Fe-$N_x$ Sites in Fe-N/C Electrocatalysts for Efficient Oxygen Reduction Reaction. *J. Am. Chem. Soc.* **2016**, *138*, 15046−15056.

(46) Ma, S.; Goenaga, G. A.; Call, A. V.; Liu, D. J. Cobalt Imidazolate Framework as Precursor for Oxygen Reduction Reaction Electrocatalysts. *Chem. - Eur. J.* **2011**, *17*, 2063−2067.

(47) Wang, X. X.; Cullen, D. A.; Pan, Y.-T.; Hwang, S.; Wang, M.; Feng, Z.; Wang, J.; Engelhard, M. H.; Zhang, H.; He, Y.; Shao, Y.; Su, D.; More, K. L.; Spendelow, J. S.; Wu, G. Nitrogen-Coordinated Single Cobalt Atom Catalysts for Oxygen Reduction in Proton Exchange Membrane Fuel Cells. *Adv. Mater.* **2018**, *30*, 1706758.

(48) Chen, Y. Z.; Wang, C.; Wu, Z. Y.; Xiong, Y.; Xu, Q.; Yu, S. H.; Jiang, H. L. From Bimetallic Metal-Organic Framework to Porous Carbon: High Surface Area and Multicomponent Active Dopants for Excellent Electrocatalysis. *Adv. Mater.* **2015**, *27*, 5010−5016.

(49) Zitolo, A.; Ranjbar-Sahraie, N.; Mineva, T.; Li, J.; Jia, Q.; Stamatin, S.; Harrington, G. F.; Lyth, S. M.; Krtil, P.; Mukerjee, S.; Fonda, E.; Jaouen, F. Identification of Catalytic Sites in Cobalt-Nitrogen-Carbon Materials for the Oxygen Reduction Reaction. *Nat. Commun.* **2017**, *8*, 957.

(50) Zang, W.; Sumboja, A.; Ma, Y.; Zhang, H.; Wu, Y.; Wu, S.; Wu, H.; Liu, Z.; Guan, C.; Wang, J.; Pennycook, S. J. Single Co Atoms Anchored in Porous N-Doped Carbon for Efficient Zinc−Air Battery Cathodes. *ACS Catal.* **2018**, *8*, 8961−8969.

(51) Shui, J.; Chen, C.; Grabstanowicz, L.; Zhao, D.; Liu, D. J. Highly Efficient Nonprecious Metal Catalyst Prepared with Metal-Organic Framework in a Continuous Carbon Nanofibrous Network. *Proc. Natl. Acad. Sci. U. S. A.* **2015**, *112*, 10629−10634.

(52) Zhao, D.; Shui, J. L.; Grabstanowicz, L. R.; Chen, C.; Commet, S. M.; Xu, T.; Lu, J.; Liu, D. J. Highly Efficient Non-Precious Metal Electrocatalysts Prepared from One-Pot Synthesized Zeolitic Imidazolate Frameworks. *Adv. Mater.* **2014**, *26*, 1093−1097.

(53) Tian, J.; Morozan, A.; Sougrati, M. T.; Lefevre, M.; Chenitz, R.; Dodelet, J. P.; Jones, D.; Jaouen, F. Optimized Synthesis of Fe/N/C Cathode Catalysts for PEM Fuel Cells: A Matter of Iron-Ligand Coordination Strength. *Angew. Chem., Int. Ed.* **2013**, *52*, 6867−6870.

(54) Proietti, E.; Jaouen, F.; Lefevre, M.; Larouche, N.; Tian, J.; Herranz, J.; Dodelet, J. P. Iron-Based Cathode Catalyst with Enhanced Power Density in Polymer Electrolyte Membrane Fuel Cells. *Nat. Commun.* **2011**, *2*, 416.

(55) Li, J.; Ghoshal, S.; Liang, W.; Sougrati, M.-T.; Jaouen, F.; Halevi, B.; McKinney, S.; McCool, G.; Ma, C.; Yuan, X.; Ma, Z.-F.; Mukerjee, S.; Jia, Q. Structural and Mechanistic Basis for the High Activity of Fe−N−C Catalysts Toward Oxygen Reduction. *Energy Environ. Sci.* **2016**, *9*, 2418−2432.

(56) Zhang, C.; Wang, Y. C.; An, B.; Huang, R.; Wang, C.; Zhou, Z.; Lin, W. Networking Pyrolyzed Zeolitic Imidazolate Frameworks by Carbon Nanotubes Improves Conductivity and Enhances Oxygen-Reduction Performance in Polymer-Electrolyte-Membrane Fuel Cells. *Adv. Mater.* **2017**, *29*, 1604556.

(57) Liu, Q.; Liu, X.; Zheng, L.; Shui, J. The Solid-Phase Synthesis of an Fe-N-C Electrocatalyst for High-Power Proton-Exchange Membrane Fuel Cells. *Angew. Chem., Int. Ed.* **2018**, *57*, 1204−1208.

(58) Cantillo, N. M.; Goenaga, G. A.; Gao, W.; Williams, K.; Neal, C. A.; Ma, S.; More, K. L.; Zawodzinski, T. A. Investigation of a Microporous Iron(iii) Porphyrin Framework Derived Cathode Catalyst in PEM Fuel Cells. *J. Mater. Chem. A* **2016**, *4*, 15621−15630.

(59) Zhu, Q.-L.; Xia, W.; Zheng, L.-R.; Zou, R.; Liu, Z.; Xu, Q. Atomically Dispersed Fe/N-Doped Hierarchical Carbon Architectures Derived from a Metal−Organic Framework Composite for Extremely Efficient Electrocatalysis. *ACS Energy Lett.* **2017**, *2*, 504−511.

(60) Chen, Y.; Ji, S.; Zhao, S.; Chen, W.; Dong, J.; Cheong, W. C.; Shen, R.; Wen, X.; Zheng, L.; Rykov, A. I.; Cai, S.; Tang, H.; Zhuang, Z.; Chen, C.; Peng, Q.; Wang, D.; Li, Y. Enhanced Oxygen Reduction with Single-Atomic-Site Iron Catalysts for a Zinc-Air Battery and Hydrogen-Air Fuel Cell. *Nat. Commun.* **2018**, *9*, 5422.

(61) Zhang, H.; Hwang, S.; Wang, M.; Feng, Z.; Karakalos, S.; Luo, L.; Qiao, Z.; Xie, X.; Wang, C.; Su, D.; Shao, Y.; Wu, G. Single Atomic Iron Catalysts for Oxygen Reduction in Acidic Media: Particle Size Control and Thermal Activation. *J. Am. Chem. Soc.* **2017**, *139*, 14143−14149.

(62) Shen, H.; Gracia-Espino, E.; Ma, J.; Zang, K.; Luo, J.; Wang, L.; Gao, S.; Mamat, X.; Hu, G.; Wagberg, T.; Guo, S. Synergistic Effects between Atomically Dispersed Fe-N-C and C-S-C for the Oxygen Reduction Reaction in Acidic Media. *Angew. Chem., Int. Ed.* **2017**, *56*, 13800−13804.

(63) Lin, Q.; Bu, X.; Kong, A.; Mao, C.; Bu, F.; Feng, P. Heterometal-Embedded Organic Conjugate Frameworks from Alternating Monomeric Iron and Cobalt Metalloporphyrins and Their Application in Design of Porous Carbon Catalysts. *Adv. Mater.* **2015**, *27*, 3431−3436.

(64) Wang, J.; Huang, Z.; Liu, W.; Chang, C.; Tang, H.; Li, Z.; Chen, W.; Jia, C.; Yao, T.; Wei, S.; Wu, Y.; Li, Y. Design of N-Coordinated Dual-Metal Sites: A Stable and Active Pt-Free Catalyst for Acidic Oxygen Reduction Reaction. *J. Am. Chem. Soc.* **2017**, *139*, 17281−17284.

(65) Zhao, R.; Liang, Z.; Gao, S.; Yang, C.; Zhu, B.; Zhao, J.; Qu, C.; Zou, R.; Xu, Q. Puffing Up Energetic Metal-Organic Frameworks to Large Carbon Networks with Hierarchical Porosity and Atomically Dispersed Metal Sites. *Angew. Chem., Int. Ed.* **2019**, *58*, 1975−1979.

(66) Zitolo, A.; Goellner, V.; Armel, V.; Sougrati, M. T.; Mineva, T.; Stievano, L.; Fonda, E.; Jaouen, F. Identification of Catalytic Sites for Oxygen Reduction in Iron- and Nitrogen-Doped Graphene Materials. *Nat. Mater.* **2015**, *14*, 937−942.

(67) Kramm, U. I.; Lefevre, M.; Larouche, N.; Schmeisser, D.; Dodelet, J. P. Correlations between Mass Activity and Physicochemical Properties of Fe/N/C Catalysts for the ORR in PEM Fuel Cell *via* $^{57}$Fe Mossbauer Spectroscopy and Other Techniques. *J. Am. Chem. Soc.* **2014**, *136*, 978−985.

(68) Roelfes, G.; Vrajmasu, V.; Chen, K.; Ho, R. Y.; Rohde, J. U.; Zondervan, C.; La Crois, R. M.; Schudde, E. P.; Lutz, M.; Spek, A. L.; Hage, R.; Feringa, B. L.; Munck, E.; Que, L., Jr. End-on and Side-on Peroxo Derivatives of Non-Heme Iron Complexes with Pentadentate Ligands: Models for Putative Intermediates in Biological Iron/Dioxygen Chemistry. *Inorg. Chem.* **2003**, *42*, 2639−2653.

(69) Jiang, W. J.; Gu, L.; Li, L.; Zhang, Y.; Zhang, X.; Zhang, L. J.; Wang, J. Q.; Hu, J. S.; Wei, Z.; Wan, L. J. Understanding the High Activity of Fe-N-C Electrocatalysts in Oxygen Reduction: Fe/$Fe_3C$ Nanoparticles Boost the Activity of Fe-$N_{(x)}$. *J. Am. Chem. Soc.* **2016**, *138*, 3570−3578.

(70) Chung, H. T.; Cullen, D. A.; Higgins, D.; Sneed, B. T.; Holby, E. F.; More, K. L.; Zelenay, P. Direct Atomic-Level Insight into the Active Sites of a High-Performance PGM-Free ORR Catalyst. *Science* **2017**, *357*, 479−484.

(71) Gokhale, R.; Chen, Y.; Serov, A.; Artyushkova, K.; Atanassov, P. Novel Dual Templating Approach for Preparation of Highly Active Fe-N-C Electrocatalyst for Oxygen Reduction. *Electrochim. Acta* **2017**, *224*, 49−55.

(72) Goenaga, G. A.; Roy, A. L.; Cantillo, N. M.; Foister, S.; Zawodzinski, T. A. A Family of Platinum Group Metal-Free Catalysts for Oxygen Reduction in Alkaline Media. *J. Power Sources* **2018**, *395*, 148−157.

(73) Venna, S. R.; Jasinski, J. B.; Carreon, M. A. Structural Evolution of Zeolitic Imidazolate Framework-8. *J. Am. Chem. Soc.* **2010**, *132*, 18030−18033.